Journal of Materials Chemistry

PAPER

Bottom-up/top-down synthesis of stable zirconium hydroxide nanophases†

Moira Ambrosi,[a] **Emiliano Fratini,**[a] **Patrizia Canton,**[b] **Stephan Dankesreiter**[c] **and Piero Baglioni**[*a]

It is well known that the structure of ZrO_2 powder synthesized by low temperature calcination of hydrous zirconia is strongly affected by the nature and properties of precursors. In the present paper, we combined a precipitation/restructuring approach (bottom-up/top-down methodology) to produce zirconium hydroxide nanoparticles that transform into stable nanophasic tetragonal zirconia by low temperature calcination. The dimension and structure of precursors could be modulated by adjusting pH. The synthetic route was investigated by Raman spectroscopy, X-Ray Diffraction, Small-Angle X-Ray Scattering and High-Resolution Transmission Electron Microscopy. The zirconium hydroxide nanoparticles represent the final product of the overall process, which starts as a bottom-up synthesis of the hydroxide gel, followed by a top-down reorganization stage. During this rearrangement, the evolving structure passes through a mass fractal that arises from the clustering of the primary zirconium hydroxide nano-units.

Introduction

Nanostructured materials possess either superior or entirely new properties with respect to the analogous bulk phases, which make them ideal for novel applications in a vast range of areas, such as medicine, electronics, biomaterials and energy production. In general, two main approaches are used to operate at the nanometer level. The first refers to the so-called "top-down" approach, according to which the nanophasic products are synthesized starting from macroscopic materials and thoroughly controlling the preparation route. In the second, the so-called "bottom-up" approach, instead, the nanomaterials are built from the molecular units by controlling and directing their self-assembly.[1]

Nanoparticles of zirconium hydroxide represent an example of nanomaterials that can be successfully produced by following both approaches. In particular, the synthesis procedure can be finely tuned in order to tailor the dimension and structure of the final product. An accurate control of the pH, for example, can lead to a peculiar structure.

The nature of precursors present in Zr(IV) solutions used to precipitate zirconium hydroxide strongly influences the structure of zirconium oxide obtained by following low temperature calcination. The hydrolysis of aqueous Zr(IV) solutions finally leads to gelatinous precipitates which represent an important step in the transformation of precursors to monoclinic or tetragonal zirconia. Quite a number of species may be formed before precipitation and, despite the wide literature on the nature and distribution of Zr(IV) chemical species present in solution, there is still controversy on their exact stoichiometry. Zr(IV) hydrolyzes even in very acidic aqueous solution to first form a tetramer which then further associates to give larger polymeric networks that can attain colloidal dimensions and, finally, settle out in a nanostructured gel form. The presence in solution of the tetramer, $[Zr_4(OH)_8(H_2O)_{16}]^{8+}$, analogous to that present in $ZrOCl_2 \cdot 8H_2O$ crystals[2] was firstly suggested by Muha and coworkers[3] and then confirmed by several authors using hydrolysis studies,[4] X-ray scattering analysis,[5,6] Raman and NMR spectroscopy,[7] and Extended X-ray Absorption Fine Structure spectroscopy (EXAFS).[8] In the tetramer, the metal atoms are arranged in a distorted square and are held together by double OH bridges along each edge; the coordination sphere of each metal atom is completed by four water molecules, two of which have been suggested to be inert and two labile on the basis of ^{17}O and ^1H NMR studies.[9] Two slowly exchanging acidic protons per Zr atom were assigned to the terminal water molecules of the tetramer; their easy dissociation produces a highly acidic solution where the formed reactive terminal hydroxyl groups condensate forming polynuclear species with higher degree of polymerization.[9,10] In fact, by dilution or by increasing the pH and/or the temperature of the tetramers' solution, a further condensation leads to the formation of more complex structures, possessing a lower charge and ranging from octamers to larger species.[7] Different structures of the octamer have been hypothesized, where tetramers are held together by hydroxo- and/or oxo-bridges. The true mechanism of octamer formation has not been disclosed yet: the octamer may form by either stacking two

[a]Department of Chemistry and CSGI, University of Florence, 50019 Sesto Fiorentino, Florence, Italy. E-mail: piero.baglioni@unifi.it; Fax: +39 055 4573036; Tel: +39 055 4573033

[b]Department of Molecular Sciences and Nanosystems, 30170 Venezia Mestre, Italy

[c]Department of Inorganic Chemistry, 93040 Regensburg, Germany

This journal is © The Royal Society of Chemistry 2012

J. Mater. Chem., 2012, **22**, 23497–23505 | 23497

tetramers on top of each other[5] where the tetramers are bound by four single hydroxo bridges, or by matching edges in which two tetrameric units are linked through two double hydroxyl bridges.[10] Upon further hydrolysis/condensation, the presence of either rod-like particles of variable length and constant cross-section,[11] or two-dimensional sheets[12] was proposed. It was found by Small Angle X-ray Scattering (SAXS)[5] that polynuclear complexes may contain different numbers of chloride ions, and a tetrameric unit with the formula $[Zr_4(OH)_8(H_2O)_{16}Cl_6]^{2+}$ and R_g = 3.8 Å was suggested as the predominant species in highly acidic Zr(IV) solutions (pH ≤ 0.3), while an octamer with the formula $[Zr_8(OH)_{20}(H_2O)_{24}Cl_{12}]$ and R_g = 5.1 Å was found to form prior to the formation of a gel/precipitate upon alkali addition or refluxing.

V. K. Ivanov et al.[13,14] studied the mesostructure evolution of hydrous zirconia xerogels by Small and Ultra-Small Angle Neutron Scattering (SANS/USANS) techniques. By increasing the pH, products exhibit a slight increase of the monomer unit radius from about 14 to about 17 Å, passing from a minimum of 13 Å at pH = 6. Above pH = 6, the synthesized xerogels show a surface fractal behavior with a characteristic dimension of 2.35 that reaches a value of 2.6 at pH = 9.

Besides zirconium hydroxides, the presence of nanostructured aggregates in liquid media is typical of other metal hydroxides and of hydrated phases, such as those found in cement-based materials. The aggregation behavior of calcium hydroxide nanoparticles was investigated by small-angle scattering techniques and it was found to strongly depend on the solvent composition. In particular, hexagonal nano-plates of about 100 nm were found to aggregate into mass fractal superstructures in 2-propanol, while more compact aggregates with surface fractal behavior were formed in ethylene glycol, where elongated structures were stabilized by face–face stacking. Displacement of ethylene glycol by 2-propanol resulted in de-aggregation towards individual units. In mixtures of the two solvents, intermediate structures were observed. This equilibrium was reversible and it could be finely tuned by adjusting the solvent composition.[15] In the case of cement pastes, calcium silicate hydrate gel represents the major phase which acts as a glue, hence determining the final compressive strength and long-term durability.[16] This gel is a nanostructured aggregate where nanometer building units organize to form mass fractal superstructures. As recently assessed by SANS,[17] each building block has an inner interlayered structure consisting of consecutive repetitions of calcium silicate and water layers. Also in this particular case, the overall aggregation process (i.e. hydration reactions), and hence the mechanical properties and long-term durability, can be tailored by changing the preparation and formulation parameters.[18]

As is evidenced by previous examples, the fine-tuning of the properties of the final product relies on the detailed control and knowledge of the structure at any stage of the bottom-up and/or top-down preparation process. The addition of a base to a Zr(IV) solution leads to a nanostructured precipitate which slowly restructures, finally giving a clear solution containing nanometer units, only when the initial molar ratio between hydroxide and Zr(IV) species, $r = [OH]_0/[Zr]_0$, is below 1. The intimate control of this combined bottom-up/top-down methodology could lead to the production of diverse exclusive structures. The purpose of this study is to develop the knowledge framework underlying the

described synthetic procedure that can be, for example, used to produce precursors of nanophasic tetragonal zirconia in a cost effective and environmental friendly way. The so-obtained nanophase is ideal for novel applications in a vast range of areas. In particular, zirconium hydroxide nanoparticles were used to successfully produce innovative and high-performing coating for porcelain stoneware tiles.[19,20] Therefore, the preparation process was structurally investigated by Raman spectroscopy, X-Ray Diffraction (XRD), SAXS and High-Resolution Transmission Electron Microscopy (HRTEM).

Materials and methods

$ZrOCl_2\cdot8H_2O$ (Aldrich, 98%), NaOH (Fluka, 97%) and NaCl (Sigma-Aldrich, 99.5%) were used without further purification. Milli-Q water was used both for preparation of samples and dialysis.

12.5 g of $ZrOCl_2\cdot8H_2O$ were dissolved in 100 mL of water to obtain a 0.39 M Zr(IV) solution. 7 mL of 5 M NaOH aqueous solution were added drop-wise under vigorous stirring at 80 °C ($r = 0.39$, pH < 1). Addition was completed within 5 minutes. A white precipitate formed which then slowly reorganized leading to a clear solution.

50 mL of the solution obtained after rearrangement of the precipitate were dialyzed against water for two weeks by using seamless cellulose tubing (12 400 MW cut-off, from Sigma-Aldrich). Dialysis was carried out in a 2 L conical flask and the water was changed every day. The pH and conductivity of water were measured and dialysis was performed until the values corresponding to Milli-Q water were reached. The temperature was kept at 25 ± 1 °C. A transparent thixotropic gel was obtained having a final pH of 5.2. The gel was stable at room temperature and was disrupted by decreasing the temperature to −15 °C, forming a white solid. An analogous gel could be obtained by dialysis of a fresh 0.39 M Zr(IV) solution obtained by dissolution of zirconyl chloride in water without any treatment with sodium hydroxide.

Samples of the Zr(IV) solutions and gel were freeze-dried for 48 h at −55 °C and 10 mTorr. The solid content of the solution was 7.43% w/w, while that of the gel was found to be 1.3% w/w. The so-obtained solids were calcined at 300 °C, 500 °C, 800 °C and 1000 °C for 2 h. Solids obtained from solutions contained different amounts of sodium chloride. NaCl was successfully removed by washing and centrifugation cycles, as demonstrated by the $AgNO_3$ test.

Raman spectra were recorded at room temperature in the range 350–650 cm^{-1} on a spectrophotometer Coherent, Innova 90/5 by using an argon laser source (1 W at 488 nm). The backscattered light from a slowly rotating NMR tube was collected and focused into a computer-controlled double monochromator (Jobin-Yvon HG2S/2000) equipped with a cooled photomultiplier (RCA C31034A) and photon-counting electronics. The spectra were calibrated to an accuracy of ±1 cm^{-1} with the characteristic lines of CCl_4. Experiments were recorded both on Zr(IV) solution obtained after reorganization of the precipitate and on equally aged solution of zirconyl chloride with the same initial concentration (0.39 M). Addition of sodium hydroxide to the Zr(IV) solution leads to the formation of a significant amount of NaCl. If we assume that the stoichiometry

of the reaction $Zr(IV)/OH^-$ is 1/2, the final concentration of the NaCl formed is 0.35 M. Thus, a zirconyl chloride solution containing 0.35 M of sodium chloride was also analyzed to investigate the sole effect of the salt.

SAXS measurements were carried out with a HECUS SWAX-camera (Kratky) equipped with a position-sensitive detector (OED 50M) containing 1024 channels of width 54 μm. Cu Kα radiation of wavelength $\lambda = 1.542$ Å was provided by a Seifert ID-3003 X-ray generator (sealed-tube type), operating at a maximum power of 2 kW. A 10 μm thick Ni-filter was used to remove the Cu Kβ radiation. The sample-to-detector distance was 275 mm. The volume between the sample and the detector was kept under vacuum during the measurements to minimize scattering from the air. The Kratky camera was calibrated in the small angle region using silver behenate ($d = 58.38$ Å).[21] Scattering curves were obtained in the q-range, $q = 4\pi/\lambda\sin\theta$, between 0.009 and 0.54 Å^{-1}, q being the scattering vector, and 2θ the scattering angle. Samples were filled either into a 1 mm glass capillary (solutions and initially formed precipitate) or into a 1 mm demountable cells having Kapton films as windows (gel formed by dialysis). The temperature was controlled by a Peltier element, with ±0.1 °C accuracy. All scattering curves were corrected for the background contribution and then iteratively desmeared using the procedure reported by Lake.[22] Error bars for each intensity point were calculated as the square root of the absolute value of intensity. The profiles were fitted by using the unified model defined by Beaucage,[23,24] which describes complex systems in terms of structural levels; each structural level concerns a Guinier regime related to an average size and a power-law regime associated to a mass or surface fractal scaling of that structural level.

X-ray diffraction measurements were performed with a powder Bruker D8 Advance Diffractometer (Bruker AXS), using Bragg–Brentano geometry and an incident radiation with $\lambda = 1.542$ Å (Cu Kα). Experiments were carried out in the range $25° \leq 2\theta \leq 65°$, with step size = 0.04°, time/step = 1 s, and voltage and current set at 40 kV and 40 mA, respectively. Diffraction peaks were assigned according to JCPDS files: monoclinic zirconia (no. 37-1484), tetragonal zirconia (no. 79-1769), and sodium chloride (no. 05-0628). The crystallite size with the corresponding errors was calculated using Topas Pro. 4 software that, after fitting of the profile and subtraction of the background, determines the crystallite size according to the Scherrer equation by measuring the full width at half of the maximum intensity (FWHM).

Transmission Electron Microscopy (TEM) analysis was performed using a JEOL JEM3010 operating at a 300 kV acceleration voltage, point to point resolution 0.17 nm at Scherzer defocus. Specimens were dispersed in 2-propanol and deposited on a holey carbon Cu-grid.

Results and discussion

Stringy looking gelatinous precipitates were formed from a zirconium aqueous solution by addition of sodium hydroxide, according to a bottom-up approach. Since the hydrolysis ratio, r, was below 1 (with $r = [OH]_0/[Zr]_0$), the precipitate restructured upon aging hence triggering a top-down process. Raman spectra recorded on $Zr(IV)$ solution obtained by simply dissolving

zirconyl chloride, with or without NaCl, and after reorganization of the precipitate are reported in Fig. 1.

The profile of the starting $Zr(IV)$ solution (without NaOH) shows bands at 450 cm^{-1}, 540 cm^{-1} and 580 cm^{-1}, indicating that an equilibrium exists between the tetrameric form, characterized by the bands at 580 cm^{-1} and at 450 cm^{-1}, and more condensed species[25] responsible for bands at 540 cm^{-1} and at 430 cm^{-1}. A Raman spectrum was also recorded on the clear solution obtained after addition of NaOH and rearrangement of the formed precipitate (sample aged for 5640 h). The species detected in solution possess a larger degree of polymerization, as is evidenced by the disappearance of bands at 450 cm^{-1} and 580 cm^{-1} and by the presence of bands at 540 cm^{-1} and 410 cm^{-1}; the latter can be assigned to soluble polymeric complexes.[26] Moreover, the band at 540 cm^{-1} is associated to vibration modes of Zr–O–Zr bonds that have been reported to connect the tetramers in the polymeric species.[27] This Raman spectrum can be assigned to precursors of gelatinous precipitates,[27] which were demonstrated to preserve the eightfold coordination of the tetrameric unit characteristic of tetragonal zirconia.[25] The presence of 0.35 M sodium chloride appears not to significantly affect the structure of the species formed, indicating that the addition of salt is not responsible for the formation of the more polymerized species detected in the aged sample.

SAXS profiles were recorded both on the starting zirconyl chloride solution and on the suspension obtained after addition of sodium hydroxide. On the latter, measurements were performed at different time intervals, starting right after the addition of the base when the white precipitate is just formed, until its complete reorganization, in order to follow the overall top-down process. The time interval needed to complete the survey covered from 4 h to 5640 h (235 days). The so-obtained scattering patterns are reported in Fig. 2 as log–log plots to evidence the presence of a power law region. Each profile is labeled with the reaction time (where $t = 0$ is the mixing time of NaOH to the starting $Zr(IV)$ solution). Two main changes are evidenced over time: the power-law exponent decreases from about 2.3 to 0, and the intensity at zero-q reduces by two orders of magnitude. The time evolution of these two quantities is reported in Fig. 3.
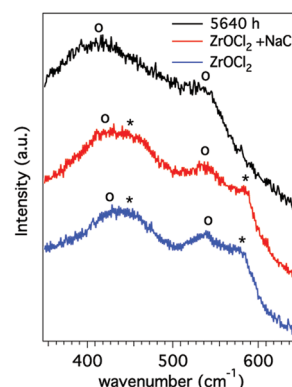
Fig. 1 Raman spectra of $Zr(IV)$ solutions: after reorganization of the precipitate (black line), aged 0.39 M $ZrOCl_2 \cdot 8H_2O$ + 0.35 M NaCl (red line) and aged 0.39 M $ZrOCl_2 \cdot 8H_2O$ (blue line). Bands characteristic of tetrameric species are labeled by asterisks, while bands ascribable to more condensed species are indicated by circles.
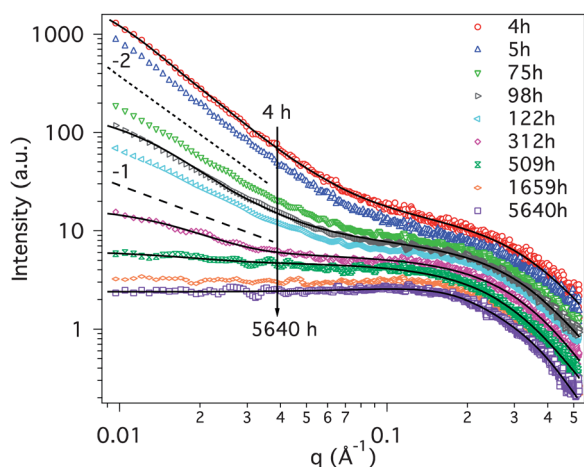
Fig. 2 SAXS profiles of samples after alkali addition with different degrees of aging (from 4 h to 5640 h). The dotted line represents the q^{-2} power-law while the broken one refers to the q^{-1} trend. Continuous lines represent the best fitting results according to the unified model (see eqn (2)) for some selected cases. Original data and the corresponding fitting have been offset for graphical purposes.
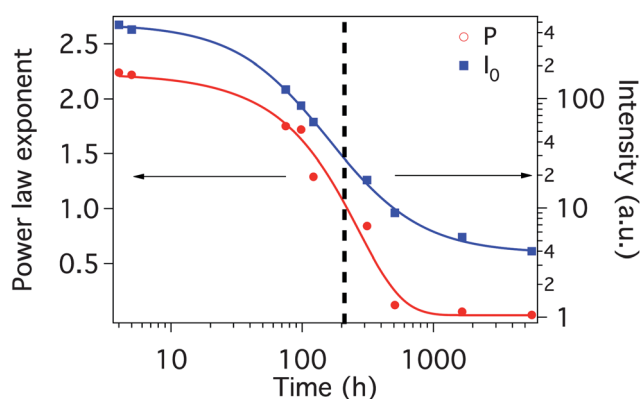
Fig. 3 Variation of power law exponent (P) and intensity at zero-q (I_0) during aging (going from 4 h to 5640 h after NaOH addition). Continuous lines are guides for the eye. The broken vertical line marks the time where the scattering object passes from fractal to non-fractal species (see explanation in the text).

SAXS probes differences in electron density between the scattering objects (*i.e.* Zr(IV) aggregates) and the solvent (*i.e.* water). As a result, the scattering profile, $I(q)$ *vs.* q, of a sample yields the different regimes of interest. Depending on the nature of the system (*i.e.* structural complexity that changes as a function of the aging time) and on the accessible q-range, the overall picture extracted by the SAXS curve can be complete or partial; inhomogeneities greater than about 50 nm and smaller than about 0.5 nm will fall outside the accessible q-range proper of a standard SAXS experiments. Ultra small angle scattering techniques as well as light scattering or even standard microscopy could be used to extract the real characteristic dimension, if greater than 50nm.

The presence of a power-law region in the scattering profile can be indicative of a fractal arrangement. In particular, the characteristic fractal dimension of the scattering object can be directly extracted from the power-law exponent, P:

$$I(q) \propto q^{-P} \tag{1}$$

in the range $1/\delta < q < 1/\sigma$. Here, δ is the size of the overall aggregate (or twice the radius of gyration, R_g) and σ is the size of the smallest units originating the fractal structure. The P exponent takes non-integer values between 1 and 4, which are strictly linked to the fractal nature of the aggregates.[28] In this regard, P allows distinguishing between mass fractals, surface fractals and non-fractals. When P falls in the range from 1 to 3, the object is a mass fractal where the fractal dimension can be defined as Dm = P. On the other hand, if P goes from 3 to 4, the object presents a surface fractal exponent which can be calculated as Ds = 6 − P hence varying from 2 to 3.

In practice, the fractal dimension quantifies how the mass M in mass fractals, or the surface area A in surface fractals, changes with the particle radius R. For mass fractal objects, which can be imagined as open, low-density structures, the mass M scales as R^{Dm}. If Dm = 3, the standard Euclidean (or non fractal) description of the mass is recovered (*i.e.* the object is a dense solid). If we move to surface fractals, which can be associated to dense solids having rough surface structures, A scales as R^{Ds}, where Ds is the surface fractal dimension. The well-known Porod's law for dense objects (Dm = 3) with smooth interfaces (Ds = 2) is obtained when P = 4.

It is important to notice that a power-law region does not necessarily indicate the presence of fractality, since particle size distributions and low-dimensional objects (like randomly distributed rods P = −1.0, randomly distributed lamellae or platelets P = −2.0) can lead to very similar results (*i.e.* apparent fractal dimensions).

An analytical model must be used to detail the aggregate structure in the nanometer scale. According to the unified fitting approach, which is very flexible and quite general,[23,24] we can assume that the SAXS intensity distribution arises from the coexistence of different structural levels:

$$I(q) = \text{bkg} + \sum_{i=1}^{N} G_i \exp\left(\frac{-q^2 R_{g_i}^2}{3}\right) + B_i \exp\left(\frac{-q^2 R_{g_{i-1}}^2}{3}\right)\left(q^*\right)^{-P_i}, \tag{2}$$

$$q^* = \frac{q}{\left[\text{erf}\left(\frac{kqR_{g_i}}{\sqrt{6}}\right)\right]^3}$$

where bkg is an instrumental background, N is the number of single polydisperse structural levels present in the investigated system, G is the Guinier pre-factor, B is a pre-factor specific to the type of power-law scattering, P is the power-law exponent already defined above for different fractal and non-fractal cases and erf( ) is the well-known error function. When the higher level is not associated with the previous smaller size level, $R_{g_{i-1}}$ is set to 0. In general $k = 1$, while in the case of mass fractal behavior k is set to 1.06 and consecutively $B_i = G_i Dm \Gamma(Dm/2)/R_{g_i}^{Dm}$. $\Gamma()$ is the well known Γ function.

SAXS curves of the evolving aggregates were fitted by using eqn (2) implemented in the Irena analysis package[29] version 2.40, running on IGOR pro 6.2. The unified approach has been limited only to two levels of complexity: the aggregates and the

sub-units. The results of the fitting are shown in Fig. 2 and the extracted parameters are reported in Table 1.
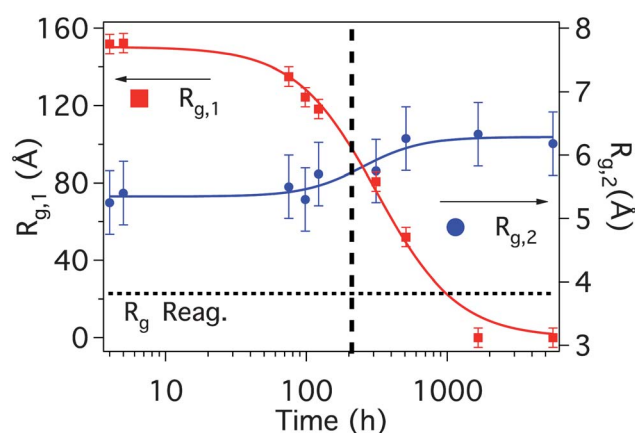
As already mentioned, addition of sodium hydroxide results into the precipitation of a white, gelatinous solid that restructures upon aging. The SAXS profile recorded after 4 hours from the addition of the base shows the presence of large aggregates, which are mass fractal in nature (Dm = 2.24) with an apparent average size R_g of about 150 Å. As time passes, the clusters rearrange and, after about one week of aging, elongated entities (rod-like structures) are formed,[11] which are about 70 Å long with a cross-section of about 5.5 Å. Afterwards, further de-aggregation takes place and a clear solution is formed within two months. The final solution contains spherical particles with a radius of gyration of about 6.2 Å, which can be hypothesized to be formed by polynuclear species obtained by hydrolysis and condensation reactions. Intermediate samples are made up of clusters with an apparent overall radius of about 50–80 Å. All SAXS profiles also show the presence of zirconium oligomeric species (5–6 Å), analogous to those present in the final clear solution, which can be assumed to represent the primary units constituting the fractal aggregates. In summary, the formed precipitate is constituted by aggregates with a mass fractal nature whose Dm ranges between 2.24 (sample analyzed after 4 h from NaOH addition) to 1.29 (sample analyzed after 122 h from NaOH addition) (Fig. 3). The associated fractal dimension agrees with the presence of highly branched clusters. The decrease of the slope indicates a time-dependent change in the structure of the hydrous zirconia particles. In fact, the clusters reorganize with time loosing part of the branches, as is evidenced by the decrease of the fractality. Eventually, linear polymeric species are formed, which then de-aggregate to form primary polynuclear particles. The size of clusters decreases during aging, changing from about 150 to 50 Å (sample analyzed after 509 h from NaOH addition). After approximately two months, clusters have totally disappeared and the only species detectable in solution are the primary units with $R_g = 6.2$ Å, whose aggregation is assumed to produce the species detected at shorter aging times (Fig. 4). In this regard, all the curves after 1659 h have been fitted using only one structural level of the unified model (i.e. primary units).

Values of the radius of gyration of the constituting units ($R_g,1$), the apparent radius of clusters ($R_g,2$), the fractal dimension (Dm) and the intensity at zero-q (I_0) at different times during aging are reported in Table 1.

Fig. 5 shows the comparison between the SAXS intensity distribution for the reagent solution (i.e. 0.39 M $ZrOCl_2 \cdot 8H_2O$
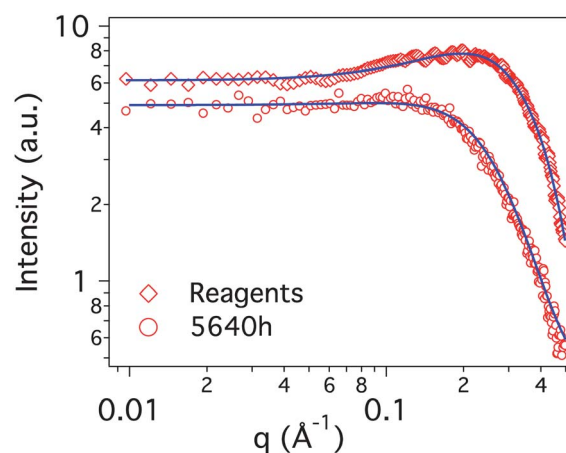

Fig. 4 Variation of radius of gyration of clusters and of constituting units during aging (going from 4 h to 5640 h after NaOH addition). Continuous lines are guides for the eye. The dotted horizontal line indicates the radius of gyration proper of the reagents (i.e. 3.8 Å). The broken vertical line marks the time where the scattering object passes from fractal to non-fractal nature.

without any addition of NaOH) and the oldest sample investigated after NaOH addition. As expected, the SAXS pattern for the starting zirconyl chloride solution without addition of sodium hydroxide did not change over time. In the case of the reagent solution, the simple one-level approach fails due to the strong interaction present between the scattering objects, which is responsible for the peak at about 0.2 Å^{-1}. In order to model this SAXS curve, a correlation term is coupled with the one-level approach.[29] The interaction could be neglected for aged solution since the addition of NaOH drastically reduces the charge of the scattering species. The reagent solution mainly contains objects with a radius of 3.8 Å, indicating that the tetramer is the predominant unit, in agreement with Raman results. The associated correlation length was about 20 Å. Very similar dimensions were extracted also using a spherical form factor (having a log-normal distribution of the average radius) coupled with a Coulomb repulsive term in the mean spherical approximation, taking into account the effective ionic strength of the solution
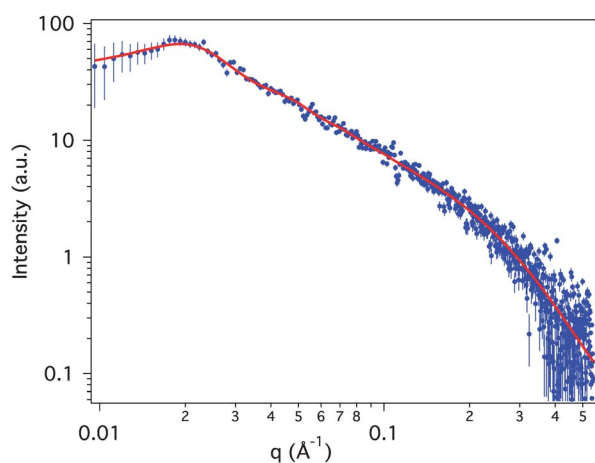
Table 1 Variation of the radius of gyration of constituting units ($R_g,1$), the apparent radius of clusters ($R_g,2$), the fractal dimension (Dm) and the intensity at zero-q (I_0) during aging

Time (h)	$R_g,1$ (Å)	$R_g,2$ (Å)	Dm	I_0 (a.u.)
4	5.3	151.8	2.24	472
5	5.4	152.3	2.22	426
75	5.5	134.9	1.75	121
98	5.3	124.4	1.72	86
122	5.7	118.2	1.29	61
312	5.8	80.7	—	18
509	6.3	52.0	—	9
1659	6.3	—	—	5
5640	6.2	—	—	4

Fig. 5 SAXS profiles of reagent solution (0.39 M $ZrOCl_2 \cdot 8H_2O$) and of sample after 5640 h from alkali addition. Continuous lines represent the best fitting results according to the models as described in the text. Original curves have been offset for graphical purposes.

and the dielectric dipole of the solvent.[30] Both approaches are approximations to the real system due to the very high concentration of the solution. As an example, we chose to report the first approach, which is consecutive to the unified model adopted to describe the de-aggregation phenomenon taking place in Zr(IV) solution after addition of NaOH.
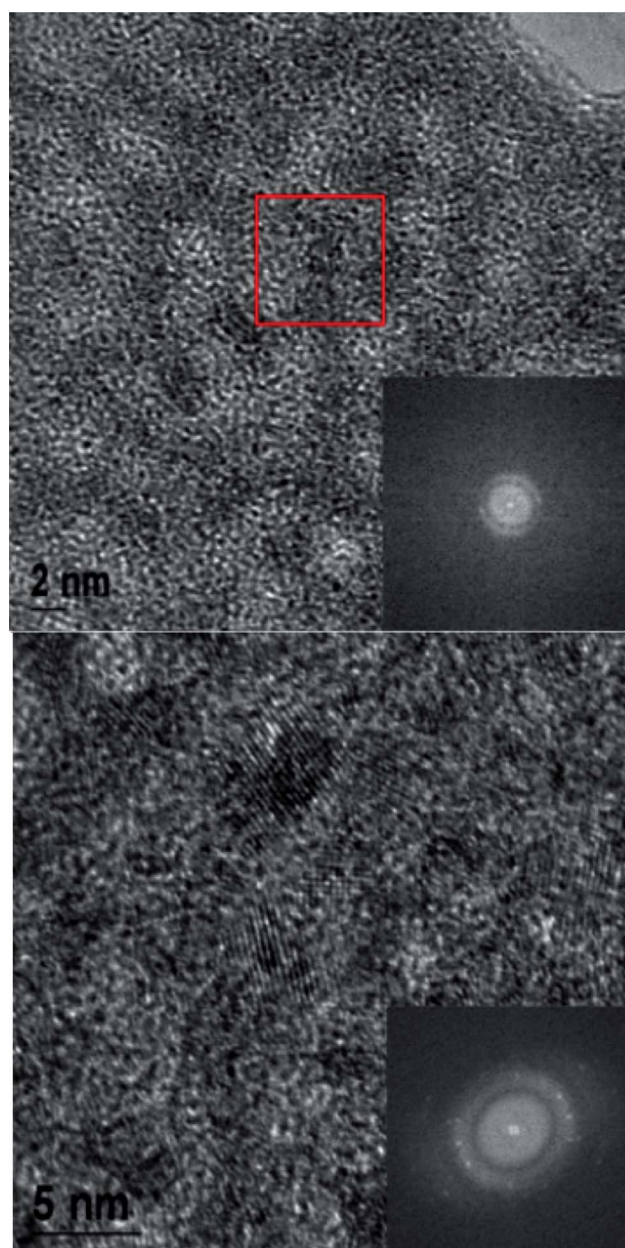
The above described primary units can in turn act as building blocks of nanostructured material obtained by a bottom-up route. Dialysis of the final clear solution, in fact, gives a nanostructured gel as a consequence of clustering/condensation of the primary units. The SAXS profile of the so obtained gel (Fig. 6) indicates the presence of primary units with a radius of gyration of 7.8 Å that aggregate to form clusters of about 70 Å with a mass fractal nature (Dm = 1.83). The system has been modeled using eqn (2) and including a correlation term to account for the peak present in the SAXS curve at about 0.02 Å^{-1}. The correlation length extracted by the fitting is 255 Å. The mass fractal dimension agrees with dimension expected by a non-equilibrium growth process where a multiparticle diffusion limited aggregate forms.[31]

HRTEM was carried out both on the aged sample (5640 h) and on the gel obtained by dialysis (Fig. 7). In both cases, crystalline domains of about 2 nm were detected as ordered regions embedded in an amorphous matrix. The crystalline areas seem to be less evident in the case of the aged sample (top). The lattice distance obtained by measuring the distances between the spots visible in the FFT on the top panel is 0.29 nm, which can indicate the presence of tetragonal zirconia. This distance can in fact be ascribed to the (101) reflection of t-ZrO$_2$. The analysis of the FFT reported on the bottom panel shows several distances that can be ascribed to reflections of tetragonal zirconia as listed in Table 2. It was reported that the presence of zirconia crystalline domains can be detected also at room temperature, after addition of alkali to Zr(IV) solutions.[6] In our case, however, the crystalline domains may also result from localized heating due to the electronic beam.

The aged solution and the gel were freeze-dried for 48 h and then calcined for 2 h at different temperatures from 300 up to 1000 °C. The so-obtained powders were analyzed by X-ray diffraction (Fig. 8).

Fig. 7 HRTEM micrographs and corresponding FFT of (top) aged sample and (bottom) hydrous zirconia gel. (Top) The FFT corresponds to the region included in the red square; (bottom) the FFT is relative to the overall image.

The freeze-dried sample (see the inset of Fig. 8, bottom panel), as well as those treated at 300 °C, shows the typical pattern of amorphous (hydrous) zirconia. The sample obtained by the aged

Table 2 Lattice distances and corresponding XRD reflections of tetragonal zirconia

Distance (nm)	Reflection
0.29	(101)
0.25	(002) or (110)
0.20	(102)
0.18	(112) or (200)
0.15	(103) or (211)

Fig. 6 SAXS profile of the gel obtained by dialysis of the aged solution. Filled blue circles represent the experimental data while continuous red line is the best fitting curve as obtained by the unified model.
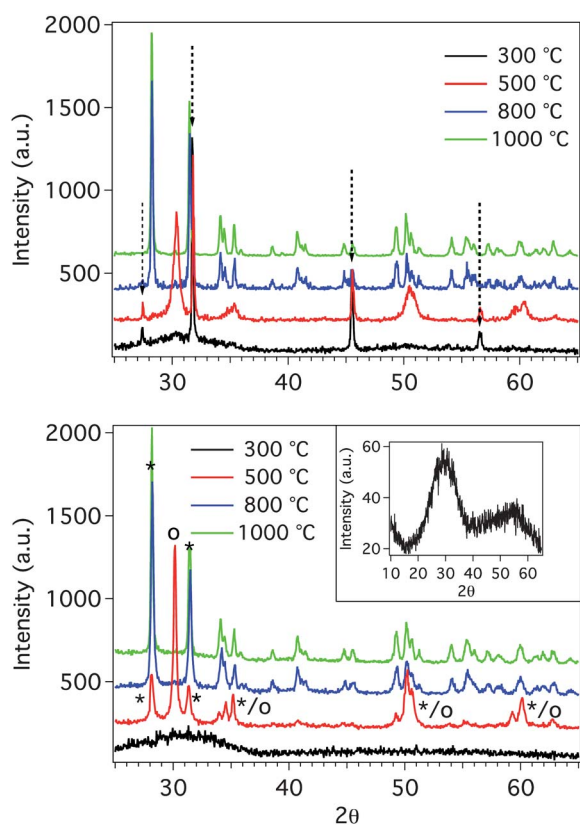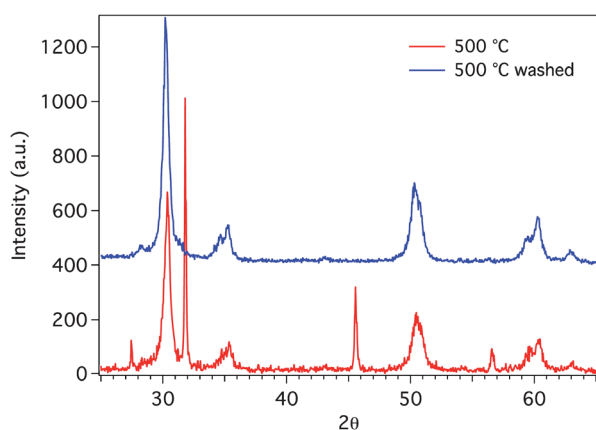
determined by SAXS. Samples treated at 300 °C appear to retain the amorphous nature, indicating that at this calcination temperature both chemical and physical water can be removed without affecting the structure. The presence of theoretically unstable amorphous zirconia at room temperature has been explained by the surface energy stabilization relative to mono-clinic zirconia for particles below 1.75 nm.[34] After treatment at
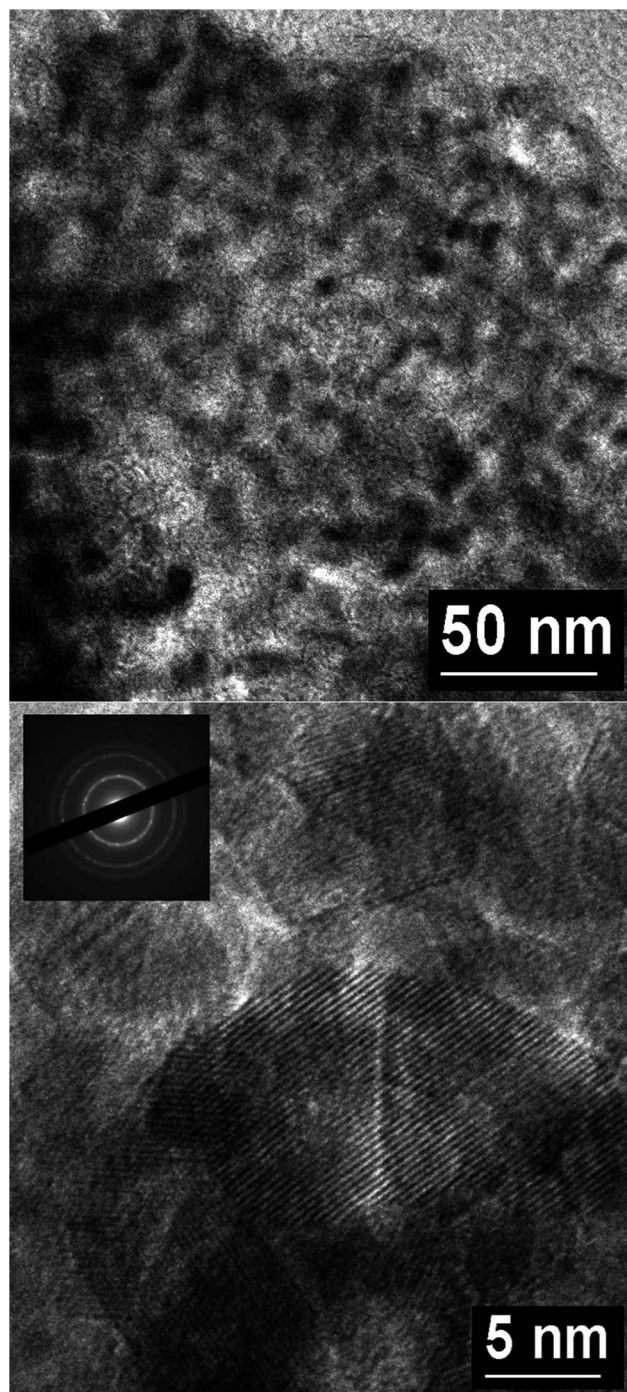

Fig. 8 XRD patterns of calcined (top) solution aged for 5640 h and (bottom) the corresponding gel obtained by dialysis. The arrows indicate Bragg reflections characteristic of NaCl, present as an impurity; asterisks indicate Bragg reflections characteristic of monoclinic zirconia; circles indicate Bragg reflections of tetragonal zirconia. The pattern of the freeze-dried gel is reported in the inset of the bottom panel. See the ESI† for standard patterns of monoclinic and tetragonal zirconia.

solution also shows peaks ascribable to NaCl (denoted by the arrows in the figure). The diffractogram of the freeze-dried sample was analyzed according to the Scherrer equation[32,33] by measuring the full width at half the maximum (FWHM) height of the peak at about 30°; a crystallite size of 7.3 Å was obtained, in good agreement with the dimension of primary units

Fig. 9 Zirconium oxide obtained after calcination of the aged solution at 500 °C, before (red) and after (blue) washing to remove impurity of NaCl.

Fig. 10 HRTEM micrographs and the corresponding Selected Area Electron Diffraction (SAED) image (inset) of zirconia obtained by calcination at 500 °C of the aged solution. The obtained solid was washed to remove NaCl.

500 °C, the aged solution transforms into pure tetragonal zirconia with a crystallite dimension of 17 nm ± 1 nm.

The gel, instead, transforms into a mixture of monoclinic and tetragonal phases. The volume fractions, v_t and v_m, of the t-ZrO$_2$ and m-ZrO$_2$ phases were calculated from the empirical formula proposed by Toraya,[35] by using the ratio between the integrated intensities of lines (111) and ($\bar{1}$11) for the monoclinic phase and of reflection (101) for the tetragonal one. Both v_t and v_m were found to be equal to 0.5. The size of the tetragonal crystallites is 36 nm ± 2 nm. After treatment at 800 °C, both formulations result in the formation of pure monoclinic zirconium oxide. Nevertheless, dimensions of the crystallites are much smaller for zirconia obtained by calcination of the gel (50 nm ± 4 nm) than for zirconia obtained from the aged solution (82 nm ± 7 nm). In both cases, the dimension of the crystallites increases by increasing the calcination temperature to 1000 °C. After treatment at 1000 °C of the aged solution, the NaCl still present after calcination at lower temperatures totally disappeared. It is worth noting that the sodium chloride could be successfully removed by simply washing the powder produced by calcination at 500 °C, so obtaining pure, stable and ultra-fine tetragonal zirconia (Fig. 9). The presence of monoclinic zirconia after calcination of the gel at 500 °C may be ascribed to the larger dimension of the nanoparticles obtained from the gel compared to those derived from the aged solution, which was suggested to stabilize the monoclinic phase. In fact, due to the lower surface energy of t-ZrO$_2$ compared to m-ZrO$_2$, the metastable tetragonal phase can be stabilized at room temperature below a certain critical size.[36–40] The increase of particle size also explains the transformation into monoclinic zirconia observed at higher temperatures as a result of the sintering process.

TEM/HRTEM analysis was performed on the final powder obtained after calcination at 500 °C of the aged solution. Experiments were recorded both before and after washing carried out to remove the impurity of NaCl. The powder was in both cases composed of nanoparticles of tetragonal zirconia with dimensions ranging from 5 to 20 nm, in agreement with results obtained by Scherrer analysis of diffraction peaks. Moreover, it is worth noting that the purification step did not lead to an increase of particle dimensions that could arise from removal of the finest portion during washing. Results of TEM/HRTEM investigations are reported in Fig. 10.

Conclusions

The properties of Zr(IV) solutions, as well as those of the gelatinous precipitates obtained by increasing the pH either through addition of sodium hydroxide or by dialysis, were thoroughly investigated. It was found that a tetramer, with R_g = 3.8 Å, is the predominant species at low pH for [Zr(IV)] = 0.39 M. After addition of sodium hydroxide, a precipitate appears to be constituted by branched clusters with a mass fractal feature. Upon aging, the precipitate rearranges first giving elongated objects and, finally, primary units with a radius of gyration of about 6 Å. By increasing the pH, these particles can associate again giving rise to a nanostructured gel. Raman spectroscopy indicated that the observed species preserve the eightfold coordination characteristic both of the tetramer and of tetragonal zirconium oxide. In fact, calcination at 500 °C of the solid

obtained after freeze-drying of the solution containing these polymer entities leads to pure tetragonal zirconia. Thus, Zr(IV) hydroxo complexes present in solution in the afore described conditions can be considered precursors of the tetragonal phase.

Stable amorphous ZrO$_2$ could be obtained by heat treatment of hydrous zirconia at 300 °C. Dimensions below a certain critical size can be invoked as responsible for stabilization of this phase at room temperature. Analogously, due to the small crystallite size (17 nm) of the ZrO$_2$ produced at 500 °C, the energetics of t-ZrO$_2$ relative to m-ZrO$_2$ stabilizes the tetragonal phase, otherwise unstable at room temperature. As expected, by increasing the calcination temperature, sintering processes take place, leading to an increase of particle dimension with formation of the monoclinic phase.

In conclusion, we developed a fine tunable process based on both a top-down and a bottom-up approach for the production of nanostructured materials. We show that the size of zirconium clusters can be controlled and finely tuned in solution both starting from a large object and decreasing their size (top-down approach) or starting from a basic zirconium unit in solution (tetramer) and growing it to form larger structures (bottom-up approach). These structures can be calcined for specific applications as coatings with enhanced properties. The important point to stress is that the fine-tuning of the precursor dimensions allows us to control the structure of the oxide forming the final coating thus expanding the range of applications. The established synthetic procedure represents a cost effective and sustainable method to prepare nanostructured zirconium hydroxide and oxide, which are ideal materials for a vast range of novel applications.

Acknowledgements

Notes and references

1 G. Cao, *Nanostructures and Nanomaterials: Synthesis, Properties and Applications*, World Scientific, 2004.
2 A. Clearfield and P. A. Vaughan, *Acta Crystallogr.*, 1956, **9**, 555.
3 G. M. Muha and P. A. Vaughan, *J. Chem. Phys.*, 1960, **33**, 194.
4 C. F. J. Baes and R. E. Mesmer, *The Hydrolysis of Cations*, John Wiley and Sons, New York, 1976.
5 A. Singhal, L. M. Toth, J. S. Lin and K. Affholter, *J. Am. Chem. Soc.*, 1996, **118**, 11529.
6 L. M. Toth, J. S. Lin and L. K. Felker, *J. Phys. Chem.*, 1991, **95**, 3106.
7 S. Hannane, F. Bertin and J. Bouix, *Bull. Soc. Chim. Fr.*, 1990, **127**, 43.
8 V. V. Kanazhevskii, V. P. Shmachkova, N. S. Kotsarenko, V. N. Kolomiichuk and D. I. Kochubei, *J. Struct. Chem.*, 2006, **47**, 860.
9 M. Aberg and J. Glaser, *Inorg. Chim. Acta*, 1993, **206**, 53.
10 P. D. Southon, J. R. Bartlett, J. L. Woolfrey and B. Ben-Nissan, *Chem. Mater.*, 2002, **14**, 4313.
11 J. A. Jutson, R. M. Richardson, S. L. Jones and C. Norman, *Mater. Res. Soc. Symp. Proc.*, 1990, **180**, 123.
12 A. Clearfield, *J. Mater. Res.*, 1990, **5**, 161.
13 V. K. Ivanov, G. P. Kopitsa, A. Ye. Baranchikov, M. Sharp, K. Pranzas and S. V. Grigoriev, *Russ. J. Inorg. Chem.*, 2009, **54**, 2091.

23504 | *J. Mater. Chem.*, 2012, **22**, 23497–23505

This journal is © The Royal Society of Chemistry 2012

14 V. K. Ivanov, G. P. Kopitsa, A. E. Baranchikov, S. V. Grigor'ev and V. M. Haramus, *Russ. J. Inorg. Chem.*, 2010, **55**, 160.

15 E. Fratini, M. G. Page, R. Giorgi, H. Cölfen, P. Baglioni, B. Demé and T. Zemb, *Langmuir*, 2007, **23**, 2330.

16 F. Ridi, E. Fratini and P. Baglioni, *J. Colloid Interface Sci.*, 2011, **357**, 255.

17 W.-S. Chiang, E. Fratini, P. Baglioni, D. Liu and S.-H. Chen, *J. Phys. Chem. C*, 2012, **116**, 5055.

18 F. Ridi, E. Fratini, P. Luciani, F. Winnefeld and P. Baglioni, *J. Phys. Chem. C*, 2012, **116**, 10887.

19 M. Ambrosi, R. Giorgi, S. Santoni, E. Fratini, N. Toccafondi and P. Baglioni, Nanogres: an innovative nanostructured zirconia-based coating for stain-resistant porcelain stoneware tiles, in preparation.

20 P. Baglioni, M. Ambrosi, L. Dei, M. Faneschi, L. Mancioli and S. Santoni, *Int. Pat.*, WO/2007/116010, PCT/EP2007/053351, 18 October 2007.

21 T. Blanton, T. C. Huang, H. Toraya, C. R. Hubbard, S. B. Robie, D. Louer, H. E. Gobel, G. Will, R. Gilles and T. Raftery, *Powder Diffr.*, 1995, **10**, 91.

22 J. A. Lake, *Acta Crystallogr.*, 1967, **23**, 191.

23 G. Beaucage, *J. Appl. Crystallogr.*, 1995, **28**, 717.

24 G. Beaucage, *J. Appl. Crystallogr.*, 1996, **29**, 134.

25 J. L. Tosan, B. Durand, M. Roubin, F. Chassagneux, M. Lucienne, F. Bertin and B. Moraweck, *J. Non-Cryst. Solids*, 1993, **160**, 167.

26 J. L. Tosan, B. Durand, M. Roubin, F. Chassagneux and F. Bertin, *J. Non-Cryst. Solids*, 1994, **168**, 23.

27 J. L. Tosan, B. Durand, M. Roubin, F. Bertin and H. Loiseleur, *Eur. J. Solid State Inorg. Chem.*, 1993, **30**, 179.

28 D. W. Schaefer and K. D. Keefer, *Phys. Rev. Lett.*, 1984, **53**, 1383.

29 J. Ilavsky and P. R. Jemian, *J. Appl. Crystallogr.*, 2009, **42**, 347.

30 J. B. Hayter and J. Penfold, *Mol. Phys.*, 1981, **42**, 109.

31 D. W. Schaefer, J. E. Martin and K. D. Keefer, in *Physics of Finely Divided Matter*, ed. N. Bocarra and M. Daoud, Springer-Verlag, Berlin, 1985.

32 H. P. Klug and L. E. Alexander, *X-ray Diffraction Procedures*, Wiley, New York, 2nd edn, 1974.

33 G. Stefanic, I. I. Stefanic and S. Music, *Mater. Chem. Phys.*, 2000, **65**, 197.

34 I. Molodetsky, A. Navrotsky, M. J. Paskowitz, V. J. Leppert and S. H. Risbud, *J. Non-Cryst. Solids*, 2000, **262**, 106.

35 H. Toraya, M. Yoshimura and S. Somiya, *J. Am. Ceram. Soc.*, 1984, C-119.

36 G. K. Chuah, S. Jaenicke, S. A. Cheong and K. S. Chan, *Appl. Catal., A*, 1996, **145**, 267.

37 R. C. Garvie, *J. Phys. Chem.*, 1965, **69**, 1238.

38 R. C. Garvie, *J. Phys. Chem.*, 1978, **82**, 218.

39 S. Shukla and S. Seal, *J. Phys. Chem. B*, 2004, **108**, 3395.

40 J. C. Valmalette and M. Isa, *Chem. Mater.*, 2002, **14**, 5098.

This journal is © The Royal Society of Chemistry 2012

J. Mater. Chem., 2012, **22**, 23497–23505 | 23505